

Surface and pseudo-surface acoustic waves piezoelectrically excited in diamond-based structures

Evgeny Glushkov, Natalia Glushkova, and Chuanzeng Zhang

Citation: *J. Appl. Phys.* **112**, 064911 (2012); doi: 10.1063/1.4754431

View online: <http://dx.doi.org/10.1063/1.4754431>

View Table of Contents: <http://jap.aip.org/resource/1/JAPIAU/v112/i6>

Published by the [American Institute of Physics](#).

Related Articles

Surface acoustic waves in pillars-based two-dimensional phononic structures with different lattice symmetries
J. Appl. Phys. **112**, 033511 (2012)

Analysis of surface acoustic wave propagation in a two-dimensional phononic crystal
J. Appl. Phys. **112**, 023524 (2012)

Scaled behavior of interface waves at an imperfect solid-solid interface
J. Appl. Phys. **112**, 024904 (2012)

Silicon edges as one-dimensional waveguides for dispersion-free and supersonic leaky wedge waves
Appl. Phys. Lett. **101**, 031904 (2012)

Spatial-temporally resolved high-frequency surface acoustic waves on silicon investigated by femtosecond spectroscopy
Appl. Phys. Lett. **101**, 013108 (2012)

Additional information on J. Appl. Phys.

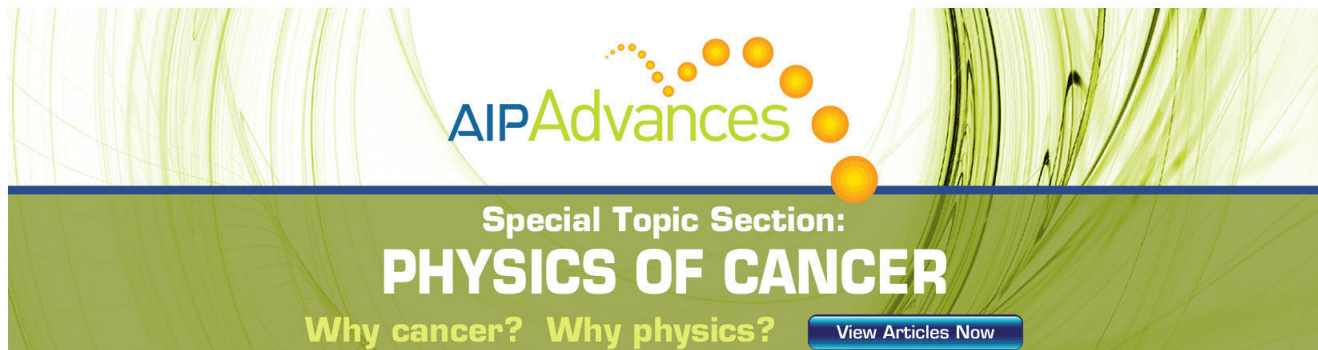
Journal Homepage: <http://jap.aip.org/>

Journal Information: http://jap.aip.org/about/about_the_journal

Top downloads: http://jap.aip.org/features/most_downloaded

Information for Authors: <http://jap.aip.org/authors>

ADVERTISEMENT

The advertisement features a green background with abstract, wavy lines. At the top, the 'AIP Advances' logo is displayed, with 'AIP' in blue and 'Advances' in green, accompanied by a series of orange dots. Below the logo, the text 'Special Topic Section: PHYSICS OF CANCER' is written in white, with 'PHYSICS OF CANCER' in a larger, bold font. At the bottom, the phrase 'Why cancer? Why physics?' is written in yellow, and a blue button with the text 'View Articles Now' is located on the right side.

AIP Advances

Special Topic Section:
PHYSICS OF CANCER

Why cancer? Why physics? [View Articles Now](#)

Surface and pseudo-surface acoustic waves piezoelectrically excited in diamond-based structures

Evgeny Glushkov,^{1,a)} Natalia Glushkova,¹ and Chuanzeng Zhang²

¹Kuban State University, Krasnodar 350040, Russia

²University Siegen, Paul-Bonatz str. 9-11, Siegen 57076, Germany

(Received 13 January 2012; accepted 24 August 2012; published online 27 September 2012)

Surface and pseudo-surface acoustic plane waves generated in two- and three-layer AlN/Diamond and AlN/Diamond/ γ -TiAl structures by a point electric source are analyzed in the mathematical framework based on the Green's matrix integral representation and guided wave asymptotics derived using the residue technique. The attention is focused on the effect of pseudo-surface-to-surface wave degeneration at certain discrete values of h/λ (h is the thickness of the piezoelectric layer and λ is the wave-length). Earlier such optimal ratios were discovered and experimentally verified for the first pseudo-surface (Sezawa) wave mode in the AlN/Diamond structure. The present research reveals this effect for higher modes as well as examines its manifestation for three-layer structures with different diamond-to-AlN thickness ratios H/h . © 2012 American Institute of Physics.

[<http://dx.doi.org/10.1063/1.4754431>]

I. INTRODUCTION

Polycrystalline diamond film layers are considered as attractive substrates for surface acoustic wave (SAW) devices operating at gigahertz frequencies because the diamond provides the highest acoustic wave velocity among all other materials.^{1–3} To enable SAW excitation by interdigital transducers (IDTs), non-piezoelectric diamond layers are covered with thin piezoelectric coatings. Among those, ZnO and AlN films are in the focus of current research as they also possess high acoustic wave velocities.^{4–10}

The geometry of such a structure composed of a diamond layer of thickness H covered by a piezoelectric film of thickness h with strip-like IDT electrodes attached to its surface is shown in Fig. 1. The diamond is underlain by a metallic half-space substrate. The electric potential p supplied via the IDT to the contact area Ω causes an electric field \mathbf{E} specified in the whole space by the electric potential φ : $\mathbf{E} = -\nabla\varphi$. Due to the piezoelectric effect, the electric field \mathbf{E} generates a coupled displacement field \mathbf{u} transmitted via the bonding interfaces from the upper piezocoating over the whole structure. The steady-state time-harmonic oscillations $\mathbf{u}e^{-i\omega t}$ and $\varphi e^{-i\omega t}$ are described by a boundary value problem (BVP) formulated with respect to their complex amplitudes \mathbf{u} and φ .

Under the assumption of y -independent in-plane displacements $\mathbf{u} = (u_x, u_z)^T$, a SAW propagation in the orthogonal to the electrodes x -direction is specified by the terms

$$\mathbf{u}_n(x, z)e^{-i\omega t} = \mathbf{a}_n(z)e^{i(k_n x - \omega t)}, \quad n = 1, 2, \dots, N, \quad (1)$$

where \mathbf{a}_n are vectors of SAW displacement amplitudes, k_n are wavenumbers, and ω is angular frequency. Hereinafter, vectors are given in bold, while scalars and matrices are not emphasized. The phase velocities $c_n = \omega/k_n$ and the wavelengths $\lambda_n = 2\pi/k_n$ are routinely expressed via the

wavenumbers k_n ; n is order number, and N is the total amount of SAWs supported by the structure at a specific frequency ω . In a multilayered half-space, N increases as ω grows and the phase velocities $c_n = c_n(\omega)$ are frequency dependent. Thus, the SAWs of form (1), including the first Rayleigh one, are undamped waves propagating with dispersion.

In addition to SAWs, layered half-space structures support so-called pseudo-surface acoustic waves (PSAWs) propagating with exponential attenuation caused by a wave energy leakage into the lower half-space.¹¹ The PSAW terms \mathbf{u}_n look similar to the SAW ones, differing only by additional damping factors $e^{-\delta_n x/\lambda_n}$

$$\mathbf{u}_n(x, z) = \mathbf{a}_n(z)e^{ik_n x}e^{-\delta_n x/\lambda_n}, \quad n = N+1, N+2, \dots \quad (2)$$

Here $\delta_n > 0$ are logarithmic decrements, indicating the order of exponential decrease of wave amplitudes \mathbf{u}_n per wavelength distances.

Due to the amplitude decay, the PSAWs were considered inappropriate for applications in acousto-electronic devices. However, it has been shown theoretically and confirmed by experimental measurements^{4,5} that at certain film-thickness-to-wavelength ratios h/λ their leakage loss might become so small that the PSAW, in fact, degenerates into a SAW, propagating with practically negligible attenuation $\delta_n \ll 1$ (hereinafter, the unsubscripted λ stands for the wavelength λ_n of a specific n -th mode considered). The use of such degenerating PSAWs seems even more attractive as their velocities are always greater than those of SAWs (the latter may not exceed the shear wave velocity c_s in the lower half-space, while the PSAW velocities $c_n = \omega/k_n$ range above c_s).

Theoretical and experimental investigations carried out for a two-layer AlN/Diamond elastic half-space^{4,5} have revealed two such points of degeneration $h/\lambda = 0.09$ and 0.15 for the first (Sezawa) PSAW mode. Besides, a three-layer AlN/Diamond/Si structure has also been considered⁶ in

^{a)}Electronic mail: evg@math.kubsu.ru.

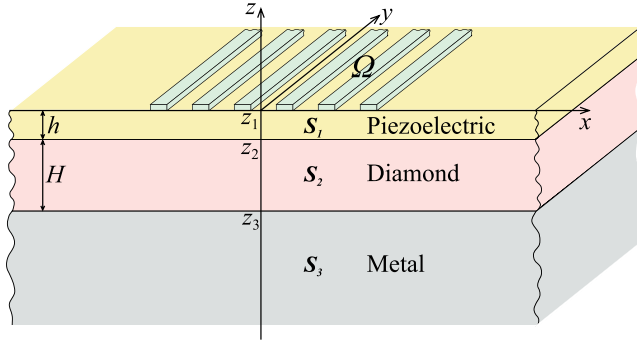


FIG. 1. Geometry of the problem.

order to determine the influence of the diamond film thickness H on the PSAW velocities and losses as compared with the two-layer half-space ($H = \infty$). The plots given there for several fixed values h/λ demonstrate an exponential decrease in the difference between the results obtained within the two-layer and three-layer models as the ratio H/λ increases. It allows one to estimate approximate values of H/λ , above which a two-layer AlN/Diamond model would be appropriate for theoretical investigations instead of a more complex three-layer model.

On the other hand, the discrepancy in the results becomes essential as h/λ and/or H/h decreases. In particular, optimal for low-loss PSAW excitation values of h/λ found in the context of a two-layer model may vary with the H/h variation. Moreover, in a three-layer model, the threshold shear wave velocity c_s in the lower half-space becomes much smaller than that in the diamond. Hence, the range of PSAW velocities stretches downward, and former real branches of SAW dispersion curves become complex. Estimation of such losses induced by the presence of a third softer substrate is also of interest.

A theoretical study of these issues in a three-layer framework has been also commenced in Ref. 10. Since the metallic γ -TiAl substrate offers advantages in the high temperature range and weight reduction, the AlN/Diamond/ γ -TiAl structure has been considered there, unlike to the three-layer composition with non-metallic silicon substrate examined in Ref. 6. The present work is a continuation of the research,¹⁰ therefore, the structures with the same γ -TiAl substrate are considered below.

The main difference from Ref. 10 is in the mathematical solution technique. A theoretical study of guided wave (GW) propagation is ordinarily based on the modal analysis technique. In this way, a term of form (1) is substituted in the homogeneous governing equations and boundary conditions of a BVP simulating wave processes without accounting for the wave source. Then the wavenumbers k_n are obtained as the roots of the characteristic equation that follows from the existence condition for a non-trivial solution. The amplitude vectors $\mathbf{a}_n(z)$ are eigensolutions (modal eigenforms) associated with the eigenvalues k_n .

This approach provides exhaustive information on the GW characteristics, except for the amplitudes \mathbf{a}_n , which, being spatial eigenforms, may only be determined to constant factors. Therefore, to find specific amplitudes of the

SAWs generated by a given source, one has to couple a modal expansion in terms (1) with a nearfield solution. The latter may be obtained, for instance, by a finite element method (FEM). However, as a whole, this way is rather cumbersome, considering additional expenses for the nearfield solution and stitching procedures.

There exists another and more natural way of accounting for wave sources modeled by non-zero boundary conditions that does not require any stitching with a nearfield solution. It is based on the Fourier transform with respect to the horizontal coordinates x and y , leading to an explicit integral representation for the wavefield generated by an electromechanical loading vector $\mathbf{q}(x,y)$ set in the contact area Ω . That loading arises in Ω when a driving voltage is applied to the IDT electrodes. The integral representation can be derived in terms of the convolution of the structure's Green's matrix $k(\mathbf{x})$, $\mathbf{x} = (x,y,z)$, with the vector $\mathbf{q}(x,y)$ or, equivalently, in the form of the inverse Fourier path integral of their Fourier symbols' product. The SAWs and PSAWs of forms (1) and (2) are obtained then as the residues from the integrand's real and complex poles, respectively. Notably, the source information automatically enters into the amplitude factors \mathbf{a}_n via the vector \mathbf{q} , thereby the amplitudes of generated GWs are uniquely defined.

That mathematical technique, referred to as integral approach, has been developed for GW propagation in 3D M -layered anisotropic structures.¹² In the present work, we use its modification for the 2D electromechanical structure considered, which is briefly described in Sec. II. Green's matrix plays a key role in this approach, therefore, Sec. III gives explicit expressions required for its independent calculation, while the results obtained for two- and three-layer structures using the model developed are discussed in Sec. IV.

II. MATHEMATICAL FRAMEWORK

Let us consider a three-layer ($M=3$) laminate structure consisting of a diamond layer of thickness H deposited on a metallic substrate and covered by a piezoelectric film of thickness h (Fig. 1). In Cartesian coordinates $\mathbf{x} = (x,y,z) \equiv (x_1,x_2,x_3)$, the structure occupies the lower half-space $-\infty < x,y < \infty$, $-\infty < z \leq 0$. The layer subdomains $S_m : z_{m+1} \leq z \leq z_m$ ($m=1,2,3; z_1=0, z_4=-\infty$) are numbered top-down. They are perfectly bonded at the interfaces $z=z_2=-h$ and $z=z_3=-(h+H)$, while the upper surface $z=z_1=0$ is stress-free everywhere except in the contact area Ω to which an IDT is attached.

In the first piezoelectric layer S_1 the complex amplitudes of the wavefields $\mathbf{u}e^{-i\omega t}$ and $\varphi e^{-i\omega t}$ obey the coupled electro-mechanical equations¹³

$$\begin{aligned} C_{ijkl} u_{l,jk} + e_{kij} \varphi_{,jk} + \rho_1 \omega^2 u_i &= 0, \quad i=1,2,3, \\ e_{jkl} u_{l,jk} - \epsilon_{jk} \varphi_{,jk} &= 0, \end{aligned} \quad (3)$$

while in the second and third ($m=2, 3$) isotropic non-piezoelectric media, the governing equations

$$(\lambda_m + \mu_m) \nabla \text{div} \mathbf{u} + \mu_m \Delta \mathbf{u} + \rho_m \omega^2 \mathbf{u} = 0, \quad (4)$$

$$\Delta \varphi = 0 \quad (5)$$

are uncoupled, with $\varphi \equiv 0$ in the metallic substrate S_3 . In addition, Eq. (5) also holds in the upper half-space $S_0 : 0 \leq z < \infty$ with respect to the potential φ in vacuum ($m=0$). Quasi-electrostatic assumption is made in this analysis.

The tensor notations in Eqs. (3) and below conventionally assume summation over identical indices and space derivatives defined by a comma. The constants C_{ijkl} , e_{ikl} and ε_{jk} are components of the elastic stiffness, piezoelectric and dielectric tensors of the coating piezomaterial, respectively; λ_m and μ_m are elastic Lamé constants of the underlying isotropic materials; ρ_m are mass densities. Together with the Lamé constants, the body wave velocities $c_{p,m} = \sqrt{(\lambda_m + 2\mu_m)/\rho_m}$ and $c_{s,m} = \sqrt{\mu_m/\rho_m}$ are also used to specify isotropic materials.

Equations (3) follow from the stress equations of motion

$$\tau_{ij,i} + \rho \omega^2 u_j = 0, \quad j = 1, 2, 3, \quad (6)$$

and the charge equation

$$D_{i,i} = 0, \quad (7)$$

after the substitution of the linear piezoelectric constitutive relations

$$\tau_{ij} = C_{ijkl} u_{k,l} + e_{kij} \varphi_{,k}, \quad D_i = e_{ikl} u_{k,l} - \varepsilon_{ik} \varphi_{,k}, \quad (8)$$

coupling the components of the stress tensor τ_{ij} and of the electric displacement vector $\mathbf{D} = (D_1, D_2, D_3)$ with the displacement and electric fields \mathbf{u} and φ . In isotropic materials relations (8) are uncoupled

$$\tau_{ij} = \lambda \operatorname{div} \mathbf{u} \delta_{ij} + \mu (u_{i,j} + u_{j,i}), \quad D_i = -\varepsilon \varphi_{,i}, \quad (9)$$

where δ_{ij} is the Kronecker symbol. Their substitution into Eqs. (6) and (7) yields separate Eqs. (4) and (5).

Perfect bonding entails continuity of the electromechanical fields across the interfaces, i.e., zero jumps of the corresponding physical quantities

$$[\mathbf{u}]_m = 0, \quad [\tau]_m = 0, \quad [\varphi]_m = 0, \quad [D_3]_m = 0, \\ z = z_m, \quad m = 2, 3, \quad (10)$$

the square brackets denote jumps at the interfaces: $[f]_m = \lim_{\varepsilon \rightarrow 0} (f|_{z=z_m-\varepsilon} - f|_{z=z_m+\varepsilon})$, $\tau = (\tau_{13}, \tau_{23}, \tau_{33})$ is a stress vector at a horizontal element.

There are two types of boundary conditions at the surface $z=0$ traditionally considered in SAW problems: the open-circuited stress-free conditions

$$\tau = 0, \quad [\varphi]_1 = 0, \quad [D_3]_1 = 0 \quad \text{at} \quad z = 0, \quad (11)$$

and the short-circuited ones

$$\tau = 0, \quad \varphi = 0 \quad \text{at} \quad z = 0. \quad (12)$$

In both cases, the corresponding BVPs are homogeneous (with zero right-hand sides in all equations and boundary conditions). The SAW modes, being their non-trivial eigen-solutions, may only be obtained up to constant factors.

Hence, the amplitudes, and so the power, of SAWs generated by a given IDT source cannot be determined without additional coupling with a quantitative nearfield solution. Indirectly the capability of an IDT to generate a specific SAW mode can be estimated via the electromechanical coupling coefficient¹⁴

$$K_n^2 = 2 \frac{c_n^o - c_n^s}{c_n^o}, \quad (13)$$

where c_n^o and c_n^s are phase velocities of the n -th mode propagating over open-circuited and short-circuited surfaces, respectively. The velocities are taken for the same fixed ratio h/λ , i.e., in general, for different frequencies.

A direct way of the IDT efficiency determination lies through the consideration of an inhomogeneous problem with non-zero boundary conditions emulating the source. Its solution should yield unique values of SAW amplitudes, providing specific source power distribution among the SAWs excited. Rigorous formulation of such a problem leads to mixed boundary conditions at the surface $z=0$. The open-circuited conditions of form (11) hold outside the contact area Ω , while the contact stresses τ and the jump $[D_3]_1$ are undefined in Ω ($[\varphi]_1 \equiv 0$ in Ω due to the metallization). Instead, a displacement vector \mathbf{w} of IDT strip contacts and a driving electric potential p have to be assigned in Ω . As a whole, it may be written as follows:

$$\mathbf{u} = \mathbf{w}, \quad \varphi = p \quad \text{for} \quad (x, y) \in \Omega, \quad z = 0, \quad (14)$$

$$\tau = (q_1, q_2, q_3), \quad [D_3]_1 = q_4 \quad \text{for} \quad -\infty < x, y < \infty, \quad z = 0. \quad (15)$$

The vector-function $\mathbf{q} = (q_1, q_2, q_3, q_4)^T$ is unknown in Ω and $\mathbf{q} \equiv 0$ for $(x, y) \notin \Omega$.

However, in general, the values of \mathbf{w} and p are also unknown. To close the problem, governing equations for IDT mechanical oscillation and for the electric circuit have to be added to substructure's equations (3)–(5). Boundary conditions (14) and (15) couples those two groups of equations, forming a more complex BVP that accounts for the IDT-substructure contact interaction. The vector \mathbf{q} , which simulates a source action upon the structure, may be obtained from this BVP only simultaneously with other unknown quantities. Nevertheless, it is possible to reduce the contact problem to separate auxiliary IDT and substrate problems based on the Green matrix concept.

Green's matrix $k(\mathbf{x})$ is introduced to give a strict quantitative information about structure's dynamic response to any surface loading \mathbf{q} . The columns $\mathbf{k}_j = (\mathbf{u}_j, \varphi_j)^T$ ($j = 1, 2, 3, 4$) of this 4×4 matrix $k = (\mathbf{k}_1 : \mathbf{k}_2 : \mathbf{k}_3 : \mathbf{k}_4)$ are formed from the solutions \mathbf{u}_j, φ_j of the substructure BVPs (3)–(5), (10) with the surface conditions

$$\tau|_{z=0} = \delta(x, y) \mathbf{i}_j, \quad [D_3]_1 = 0 \quad \text{for} \quad j = 1, 2, 3, \\ \tau|_{z=0} = 0, \quad [D_3]_1 = \delta(x, y) \quad \text{for} \quad j = 4, \quad (16)$$

instead of Eqs. (15). Here \mathbf{i}_j are basis vectors and $\delta(x, y)$ is Dirac's delta-function; i.e., the columns \mathbf{k}_j specify the structure's response to the concentrated loads applied at the origin

$\mathbf{x}=0$ along the coordinate axis directions ($j=1,2,3$) and to the point jump of the normal electric displacement component D_3 ($j=4$). Any electromechanical wavefield $\mathbf{v} = (\mathbf{u}, \varphi)^T$ associated with a specific loading vector \mathbf{q} can be represented as a convolution of k with \mathbf{q} , or, alternatively, via their Fourier symbols K and \mathbf{Q}

$$\begin{aligned} \mathbf{v}(\mathbf{x}) &= \iint_{\Omega} k(x - \xi, y - \eta, z) \mathbf{q}(\xi, \eta) d\xi d\eta \\ &= \frac{1}{4\pi^2} \int_{\Gamma_1} \int_{\Gamma_2} K(\alpha_1, \alpha_2, z) \mathbf{Q}(\alpha_1, \alpha_2) e^{-i(\alpha_1 x + \alpha_2 y)} d\alpha_1 d\alpha_2. \end{aligned} \quad (17)$$

The Fourier symbols result from the transformation \mathcal{F}_{xy} over the horizontal coordinates x and y

$$K(\alpha_1, \alpha_2, z) = \mathcal{F}_{xy}[k] \equiv \int_{-\infty}^{\infty} \int_{-\infty}^{\infty} k(x, y, z) e^{i(\alpha_1 x + \alpha_2 y)} dx dy,$$

and similarly for $\mathbf{Q} = \mathcal{F}_{xy}[\mathbf{q}]$. The last double integral in Eq. (17) is actually the inverse transformation \mathcal{F}_{xy}^{-1} of the Fourier-transform domain solution $\mathbf{V} = K\mathbf{Q}$ to the auxiliary BVP (3)–(5), (10), and (15). The integration paths Γ_1 and Γ_2 go along the real axes, deviating from them into the complex planes α_1 and α_2 for rounding real poles of the integrand $\mathbf{V}(\alpha_1, \alpha_2, z)$.

In the contact area Ω , the augmented by the electric potential displacement vector $\mathbf{v} = (\mathbf{u}, \varphi)$ must coincide with the IDT boundary displacement and electric characteristics entering in contact conditions (14): $\mathbf{v}(x, y, 0) = (\mathbf{w}, p)^T$. Therefore, a substitution of integral representation (17) with $z=0$ into these conditions leads to a closed integro-differential problem with respect to unknown IDT characteristics and \mathbf{q} . The differential equations of IDT motion are generally simpler than those for the substructure $z \leq 0$, while the electromechanical response of the latter is strictly accounted for via Green's matrix. An example of such technique implementation for flexible piezoelectric patch actuators bonded to an elastic layer may be found in Ref. 15. If \mathbf{w} and p are known, e.g., from experimental measurements, the problem is reduced to the Wiener-Hopf integral equation with respect to the only unknown \mathbf{q} :

$$\begin{aligned} K\mathbf{q} &\equiv \iint_{\Omega} k(x - \xi, y - \eta, 0) \mathbf{q}(\xi, \eta) d\xi d\eta = \mathbf{f}(x, y) \quad (x, y) \in \Omega, \\ \mathbf{f} &= \mathbf{v}(x, y, 0) = (\mathbf{w}, p)^T. \end{aligned} \quad (18)$$

As soon as \mathbf{q} is determined, only Eq. (17) is enough for a quantitative wave analysis in the structure. Since the present work is focused on SAW/PSAW characteristics, which do not dependent on source parameters, a self-dependent problem of IDT modeling is out of its scope. We assume that \mathbf{q} is prescribed, using a point-source IDT model in the numerical examples below. Nevertheless, even with such a simple source, the mathematical model developed yields a worthwhile information about the source energy distribution among the excited GWs.

A closed representation for cylindrical GWs generated by the load \mathbf{q} can be derived from Eq. (17) in terms of residues and Hankel functions in the same way as it was accomplished in Ref. 12. That asymptotic representation allows one to analyze GW radiation in any directions. With a comb IDT under consideration, a plane wave propagation in the direction orthogonal to the comb contacts is of prime concern. Hence, a 2D statement with respect to the y -independent in-plane oscillation $\mathbf{v}(x, z)$ may be considered instead of the full 3D statement above.

In the 2D framework, only the Fourier transform \mathcal{F}_x with respect to x is applied and the wavefield \mathbf{v} is described by the single path integral

$$\mathbf{v}(x, z) = \frac{1}{2\pi} \int_{\Gamma} K(\alpha, z) \mathbf{Q}(\alpha) e^{-i\alpha x} d\alpha. \quad (19)$$

The matrix K here is a special case of that in Eq. (17) with $\alpha = \alpha_1$, and $\alpha_2 = 0$ and $\mathbf{Q} = \mathcal{F}_x[\mathbf{q}(x)]$. In accordance with the residue technique, the integration contour Γ (Fig. 2) can be closed upward or downward for $x < -a$ and $x > a$, respectively (a is the half-width of the contact domain Ω : $|x| < a$). It brings Eq. (19) to the sum of residues from the poles $\pm \zeta_n$ of K elements plus the remaining integrals over the banks of the vertical cuts C_j^{\pm} , $j=1,2$, drawn in the complex α -plane from the branch points $\pm \kappa_j$ to infinity (Fig. 2):

$$\mathbf{v}(x, z) = \sum_{n=1}^{\infty} \mathbf{v}_n(z) + \frac{1}{2\pi} \sum_{j=1}^2 \int_{C_j^{\pm}} \mathbf{V}(\alpha, z) e^{-i\alpha x} d\alpha, \quad (20)$$

$$\mathbf{v}_n = (\mathbf{u}_n, \varphi_n)^T = \mathbf{a}_n e^{i\zeta_n |x|}, \quad \mathbf{a}_n(z) = \mp \text{res} K(\alpha, z) \big|_{\alpha=\mp \zeta_n} \mathbf{Q}(\mp \zeta_n),$$

the upper and lower signs are for $x > a$ and $x < -a$, respectively. The cuts assure the unique analytical continuation from the real axis onto the single-valued surface sheet of the Riemann manifold induced by the branch points $\pm \kappa_j$. These cuts exclude the sheets which points α yield unphysical wave phenomena (so-called unphysical sheets), selecting the one that provides physically appropriate wave parameters (a physical sheet). The poles ζ_n are located in the upper half-plane $\text{Im} \alpha \geq 0$ above Γ and arranged in order of increasing imaginary parts, i.e., $\text{Im} \zeta_{n+1} \geq \text{Im} \zeta_n$. The centrally symmetric to ζ_n poles $-\zeta_n$ lie beneath Γ . A limited number of the first poles ζ_n , $n=1,2,\dots,N$, are real. They are located on the

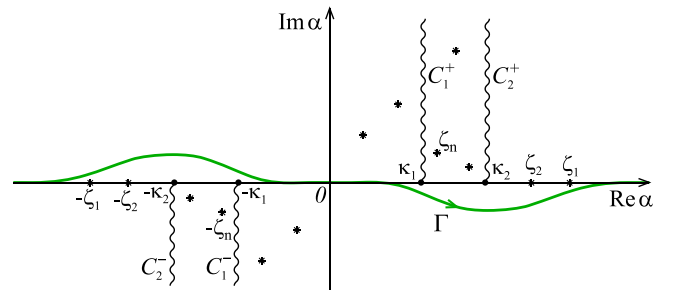


FIG. 2. Integration contour Γ , branch points $\pm \kappa_j$, cuts C_j^{\pm} and poles $\pm \zeta_n$ in the complex plane α . The star symbols schematically show possible location of real (SAW) and complex (PSAW) poles ζ_n on the right and left of κ_2 , respectively.

right of the branch point κ_2 . The corresponding terms \mathbf{u}_n in sum (20) are undamped SAWs, while complex ζ_n , located not far from the real axis on the left of the cut C_2^+ , yield PSAWs propagating with the exponential attenuation $e^{-\text{Im} \zeta_n |x|}$ as $|x| \rightarrow \infty$. Their number is also limited, while the rest of the infinite set of ζ_n are featured by large, rapidly growing with n , imaginary parts.

The phase velocities, wave lengths and logarithmic decrements of the GW modes \mathbf{v}_n are

$$c_n = \omega / \text{Re} \zeta_n, \quad \lambda_n = 2\pi / \text{Re} \zeta_n \quad \text{and} \quad \delta_n = 2\pi \text{Im} \zeta_n / \text{Re} \zeta_n. \quad (21)$$

The branch points $\kappa_1 = \omega / c_p$ and $\kappa_2 = \omega / c_s$ are specified by the velocities of P and S (longitudinal and transverse) body waves propagating in the lower half-space S_M ($c_p = c_{p,M}$, $c_s = c_{s,M}$, $M=2$ or 3 in a two- or three-layer model, respectively). Accordingly, the integrals over the branch cuts C_j^\pm yield body waves.

The dependence of GW amplitudes on the depth z is specified by the vector-functions $\mathbf{a}_n(z)$. Up to constant factors they coincide with modal eigenforms obtained using conventional modal analysis technique, e.g., by the matrix method.¹⁶ Unlike the eigensolutions, the amplitude functions \mathbf{a}_n are controlled by the source factors $\mathbf{Q}(\mp \zeta_n)$ that uniquely fix their values, while the structure determines the GW shapes via the matrix K . The algorithm of its calculation is briefly described in Sec. III.

III. GREEN'S MATRIX

Fourier-transformed Eqs. (3) can be compactly written in the form

$$C_{ijkl} \alpha_j \alpha_k U_l + e_{kij} \alpha_j \alpha_k \Phi - \rho \omega^2 U_i = 0, \quad i = 1, 2, 3, \\ e_{ikl} \alpha_i \alpha_k U_l - \varepsilon_{ik} \alpha_i \alpha_k \Phi = 0. \quad (22)$$

The multiplier $-i\alpha_3$ is treated here as an operator notation for the derivative $\partial/\partial z$ in accordance with the property $\mathcal{F}_x[\frac{\partial^n \mathbf{v}}{\partial z^n}] = (-i\alpha_3)^n \mathbf{V}(\alpha)$, $\alpha = (\alpha_1, \alpha_2, \alpha_3)$; $\mathbf{V}(\alpha) = \mathcal{F}_x[\mathbf{v}]$ is the transformation with respect to all spatial variables x_1, x_2, x_3 . Similarly, Eqs. (9) for the stress and electric displacement components take the following forms in the Fourier-transform domain

$$T_{i3} = -i\alpha_k C_{i3jk} U_j - i\alpha_k e_{ki3} \Phi, \quad D_3 = -i\alpha_k e_{3kj} U_j + i\alpha_k \varepsilon_{3k} \Phi. \quad (23)$$

In this way, the transformed BVP can be written in the matrix form

$$[B(\alpha, z) - \rho \omega^2 I_3] \mathbf{V}(\alpha_1, \alpha_2, z) = 0, \quad (24)$$

$$T_1(\alpha) \mathbf{V}(\alpha_1, \alpha_2, z)|_{z=0} = \mathbf{Q}(\alpha_1, \alpha_2), \quad (25)$$

$$[\mathbf{V}]_m = 0, \quad [T\mathbf{V}]_m = 0, \quad m = 2, 3, \quad (26)$$

where $I_3 = \text{diag}(1, 1, 1, 0)$,

$$B = [b_{ij}]_{i,j=1}^4 = \begin{bmatrix} B_s & B_{se} \\ B_{es} & B_e \end{bmatrix}, \quad (27)$$

$$B_s : b_{ij} = C_{iljk} \alpha_k \alpha_l, \quad i, j = 1, 2, 3;$$

$$B_{se} : b_{i4} = e_{kij} \alpha_j \alpha_k, \quad i = 1, 2, 3;$$

$$B_{es} : b_{4j} = e_{ikj} \alpha_i \alpha_k, \quad j = 1, 2, 3;$$

$$B_e : b_{44} = -\varepsilon_{ik} \alpha_i \alpha_k,$$

and

$$T = [T_{ij}]_{i,j=1}^4 = \begin{bmatrix} T_s & T_{se} \\ T_{es} & T_e \end{bmatrix} \quad (28)$$

$$T_s : T_{ij} = -i\alpha_k C_{i3jk}, \quad i, j = 1, 2, 3;$$

$$T_{se} : T_{i4} = -i\alpha_k e_{ki3}, \quad i = 1, 2, 3;$$

$$T_{es} : T_{4j} = -i\alpha_k e_{3kj}, \quad j = 1, 2, 3;$$

$$T_e : T_{44} = i\alpha_k \varepsilon_{3k}.$$

The matrix T_1 in Eq. (25) is of the form (28) but with the additional term $-\varepsilon_0 \alpha$ in the T_{44} component, $\varepsilon_0 = 8.85419 \text{ F/m}$ is the vacuum dielectric constant and $\alpha = \sqrt{\alpha_1^2 + \alpha_2^2}$. This term appears because the boundary condition (15) involves the jump $[D_3]_1$ between the D_3 values in the piezoelectric coating S_1 and in the vacuum domain S_0 . In the isotropic domains S_2 and S_3 , the matrices B and T are block-diagonal ones with zero off-diagonal solid-electric and electric-solid blocks: $B_{se} = T_{se} = 0$ and $B_{es} = T_{es} = 0$.

Non-trivial solutions to the ordinary differential equations (24) are sought for in the form $\mathbf{V} = \mathbf{p} e^{\gamma z}$. Its substitution into Eq. (24) leads to the matrix eigenvalue problem

$$[B(\alpha) - \rho \omega^2 I_3] \mathbf{p} = 0, \quad (29)$$

in which $\alpha_3 = i\gamma$. The characteristic equation

$$\det[B(\alpha_1, \alpha_2, i\gamma) - \rho \omega^2 I_3] = 0 \quad (30)$$

has 8 roots γ_k which may be divided into two groups: $\gamma_j = \sigma_j$ and $\gamma_{j+4} = -\sigma_j$ ($j = 1, 2, 3, 4$) arranged as follows:

$$\text{Re } \sigma_4 > \text{Re } \sigma_1 > \text{Re } \sigma_2 \geq \text{Re } \sigma_3 \geq 0 \quad \text{and}$$

$$\text{Im } \sigma_3 \leq \text{Im } \sigma_2 \leq \text{Im } \sigma_1 \leq \text{Im } \sigma_4 \leq 0 \quad \text{for real } \alpha_1, \alpha_2.$$

In the special case of isotropic materials, i.e., for subdomains S_2 and S_3 , the roots are $\sigma_j = \sqrt{\alpha^2 - \kappa_j^2}$, $j = 1, 2, 3$, where $\alpha^2 = \alpha_1^2 + \alpha_2^2$, κ_1 and $\kappa_2 \equiv \kappa_3$ are wave numbers of longitudinal and transversal body waves in the elastic materials, while $\sigma_4 = \sqrt{\alpha^2}$ is associated with the uncoupled Eq. (5) for the electric potential φ . Such root regulation is significant for the rejection of unphysical terms with the exponentials $e^{-\sigma_j z}$ not meeting the attenuation and radiation conditions in the lower half-space S_3 . In the upper layers S_1 and S_2 , the root ordering is also used. It allows one to avoid numerical instabilities caused by growing exponentials by taking general solutions for these layers in the form

$$\mathbf{V} \equiv \mathbf{V}_m = \sum_{j=1}^4 [t_m^{(j)} \mathbf{p}_j e^{\sigma_j(z-z_m)} + t_m^{(4+j)} \mathbf{p}_{4+j} e^{-\sigma_j(z-z_{m+1})}], \\ z \in S_m, \quad m = 1, 2, \quad (31)$$

where \mathbf{p}_k are eigenvectors (non-trivial solutions to Eq. (29)) associated with the roots $\pm\sigma_j$, and $t_m^{(k)}$ are unknown coefficients.

In the lower half-space

$$\mathbf{V}_3 = \sum_{j=1}^3 t_3^{(j)} \mathbf{p}_j e^{\sigma_j(z-z_3)}, \quad z \in S_3. \quad (32)$$

Here $t_3^{(4+j)} = 0$ due to the radiation conditions, and in addition $t_3^{(4)} = t_3^{(8)} = 0$ since $\varphi \equiv 0$ in the metallic substrate S_3 .

The unknown coefficients $t_m^{(j)}$ assembled into the column vector $\mathbf{t} = (\mathbf{t}_1, \mathbf{t}_2, \mathbf{t}_3)^T$ of length 19 ($\mathbf{t}_m = (t_m^{(1)}, \dots, t_m^{(8)})$, $m = 1, 2$ and $\mathbf{t}_3 = (t_3^{(1)}, t_3^{(2)}, t_3^{(3)})$) are obtained from the system of linear algebraic equations

$$A \mathbf{t} = \mathbf{f}, \quad \mathbf{f} = (\mathbf{Q}, 0, \dots, 0)^T, \quad (33)$$

which follows from the substitution of expressions (31) and (32) into the boundary conditions (25) and (26).

Since the Green matrix $k(\mathbf{x})$ is constructed from the solutions $\mathbf{v} = \mathbf{k}_j(\mathbf{x})$ corresponding to point sources (16), the columns \mathbf{K}_j of the matrix $K(\alpha_1, \alpha_2, z)$ have the same forms (31) and (32) as the vector $\mathbf{V}(\alpha_1, \alpha_2, z)$ but with the coefficients $t_m^{(j)}$ found from the system (33) for the four right-hand side vectors $\mathbf{f} = (\mathbf{e}_j, 0, \dots, 0)^T$, where $\mathbf{e}_j = (\delta_{1j}, \delta_{2j}, \delta_{3j}, \delta_{4j})$, $j = 1, \dots, 4$.

IV. RESULTS AND DISCUSSION

A. Material parameters

For the sake of results' comparability, a two-layer AlN/Diamond structure ($M=2$, $H=\infty$) with the same material parameters as in Refs. 4, 5, and 8 has been considered at first. In both cases $M=2$ and $M=3$, the GW expansion is obtained in terms of sum (20). The only difference is in the matrix K representation. In the case $M=2$, the general solution \mathbf{V}_2 in the diamond half-space S_2 is of form (32) with the unknown vector $\mathbf{t}_2 = (t_2^{(1)}, t_2^{(2)}, t_2^{(3)})$, so that the system (33) becomes of the size 11×11 ($\mathbf{t} = (\mathbf{t}_1, \mathbf{t}_2)^T$, \mathbf{t}_1 is as above).

In the case $M=3$, the properties of the additional metallic half-space S_3 have been taken for a γ -TiAl alloy, the same as in Ref. 10. The material constants used in the numerical examples below are given in Table I. The piezocoating AlN is transversally isotropic, its elastic properties are specified by five elastic constants, while the remaining non-zero constants $C_{22} = C_{11}$, $C_{23} = C_{13}$ and $C_{66} = \frac{1}{2}(C_{11} - C_{12})$ are not independent. The constants C_{ijkl} and e_{ijk} are compactly expressed here as two-index elements $C_{\alpha\beta}$ and $e_{i\gamma}$ in accordance with Voigt's convention

$$\begin{array}{cccccc} ij & \text{or} & kl & \text{or} & jk & : & 11 & 22 & 33 & 23 & 13 & 12 \\ \alpha & \text{or} & \beta & \text{or} & \gamma & : & 1 & 2 & 3 & 4 & 5 & 6 \end{array}$$

The anisotropy results in different velocities of body wave propagation in the horizontal direction ($c_p = \sqrt{C_{11}/\rho} = 10\,287$ m/s, $c_s = \sqrt{C_{44}/\rho} = 6\,016$ m/s) and along the Oz axis ($c_p = \sqrt{C_{33}/\rho} = 11\,008$ m/s, $c_s = \sqrt{C_{66}/\rho} = 5\,809$ m/s). The body wave velocities of the isotropic materials are

$$\begin{array}{ll} c_{p,2} = 18\,120 \text{ m/s}, & c_{s,2} = 12\,320 \text{ m/s} \quad \text{for Diamond} \\ c_{p,3} = 7\,546 \text{ m/s}, & c_{s,3} = 4\,035 \text{ m/s} \quad \text{for } \gamma\text{-TiAl.} \end{array}$$

It is pertinent to note once again that the threshold velocity $c_s = c_{s,M}$, separating SAW and PSAW ranges of GW velocities c_n , considerably differs for the cases $M=2$ ($c_s = 12\,320$ m/s) and $M=3$ ($c_s = 4\,035$ m/s). Besides, an additional variable geometrical parameter H appears in the case $M=3$. To demonstrate the influence of the diamond-to-piezoelectric layer-thickness ratio H/h on the effects revealed in the context of the two-layer model, the results for three-layer structures with the high, medium and small ratios $H/h = 10, 5$ and 2 are discussed in Sec. IV C.

B. Two-layer AlN/Diamond structure

Whereas the phase velocities c_n and the coupling coefficients K_n^2 of several first SAW modes have been already well studied (e.g., Ref. 8), only the complex branch of the second (Sezawa) mode has been examined in detail in order to reveal the effect of PSAW-to-SAW degeneration (i.e., to find h/λ for which δ_n becomes very small).^{4,5} Notice that we number the modes starting from $n=1$, in accordance with the pole numbering in Eq. (20), unlike the frequently used numbering starting from $n=0$.

The dispersion curves of the first ten GW modes propagating in the AlN/Diamond structure in the frequency range $0 < h/\lambda < 2$ are shown in Fig. 3. All the velocities smoothly decrease as h/λ increases. The first curve c_1 is for the fundamental Rayleigh mode. It starts from the value $c_R = 10\,920$ m/s at $h/\lambda = 0$ and tends to $c_R = 5\,608$ m/s as $h/\lambda \rightarrow \infty$. These values coincide with the velocities c_R of the classical Rayleigh wave in the homogeneous half-spaces with the diamond and AlN properties, respectively. This curve is entirely situated in the SAW zone ($c_1 < c_s$), while the velocities c_n of all other SAW modes reach the threshold level $c_s = 12.32$ km/s at certain values of h/λ if tracing them from right to left. Then the corresponding poles ζ_n pass through the branch point κ_2 and come out from the real axis into the complex α -plane. The even ones get on the physical Riemann surface sheet, while the

TABLE I. Material parameters.

	C_{11} (GPa)	C_{12}	C_{13}	C_{33}	C_{44}	e_{15} (C/m ²)	e_{31}	e_{33}	ε_{11} (pF/m)	ε_{33}	ρ (kg/m ³)
AlN	345	125	120	395	118	-0.48	-0.58	1.55	80	95	3260
Diamond	1153				533				55	55	3512
γ -TiAl	222.1				63.5						3900

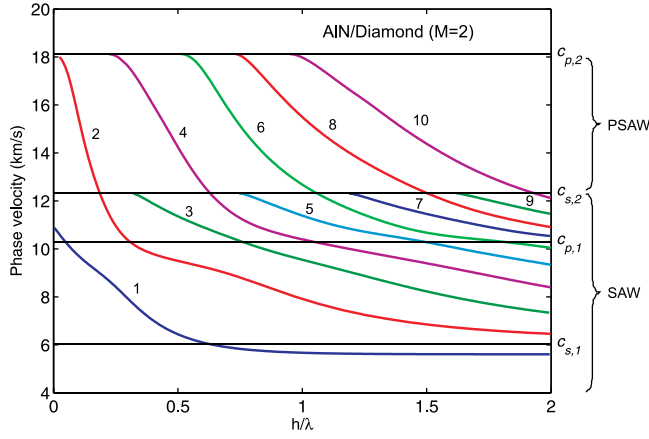


FIG. 3. SAW ($c_n < c_{s,2}$) and PSAW ($c_n > c_{s,2}$) phase velocities c_n in the AIN/Diamond structure ($H = \infty$).

odd ones go off onto the unphysical sheet ceasing contribution into GW expansion (20). Therefore, in the figure they are not drawn above c_s . The real sections of the curves shown in Fig. 3 coincide with the known plots of higher SAW modes, e.g., with the curves of the first five modes presented in Refs. 8 and 10.

The top and bottom subplots of Fig. 4 depict coupling coefficients K_n^2 versus h/λ for all the ten modes of Fig. 3 (both for SAW and PSAW parts). The parts of the first five ones

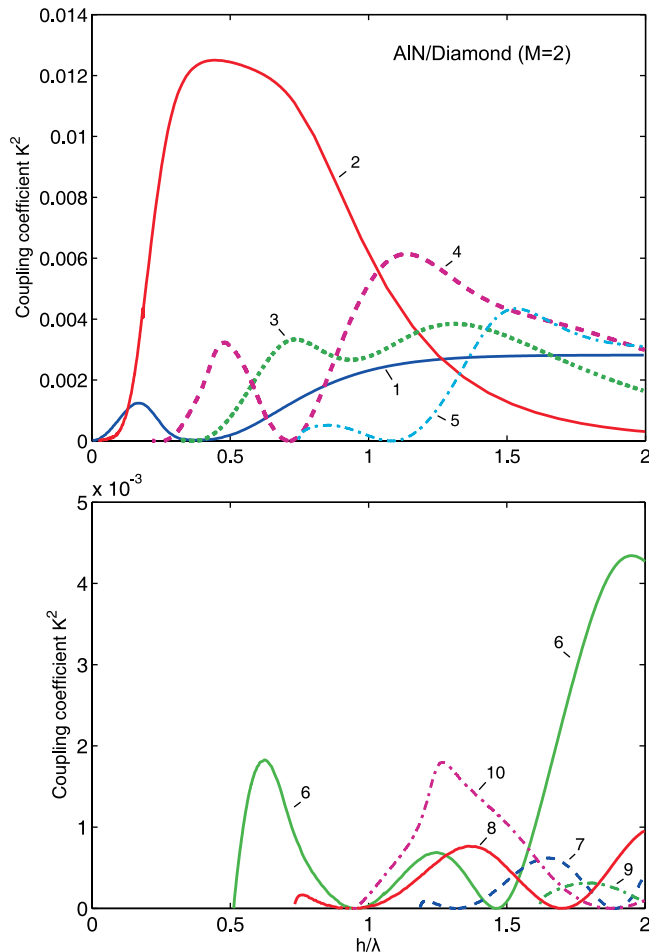


FIG. 4. Coupling coefficients K_n^2 for the GW modes shown in Fig. 3.

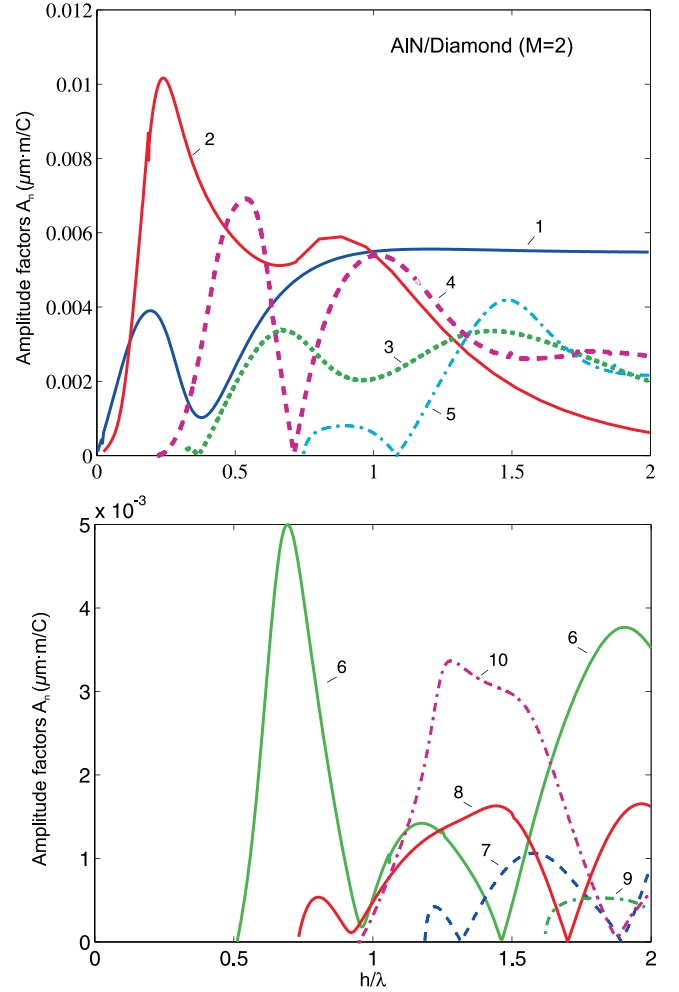


FIG. 5. Amplitude factors A_n of the same GWs as in Fig. 3 generated by the point electric source $[D_3]_1 = d\delta(x)$; $h = 4.3 \mu\text{m}$.

corresponding to real c_n (Fig. 4, top) also coincide with the SAW coupling coefficients presented in Ref. 8. Since the coupling coefficients denote structure's ability to produce various GWs in response to an applied voltage, it is interesting to compare them with plots of the GW amplitudes a_n in expression (20) obtained for a prescribed source vector \mathbf{q} . Figure 5 displays the relative amplitude factors $A_n = |\hat{\mathbf{a}}_n|/d$ ($\mu\text{m} \cdot \text{m}/\text{C}$) for the GWs generated by the point electric source $\mathbf{q} = (0, 0, 0, q_4)^T$, $q_4 = d\delta(x)$ (vectors $\hat{\mathbf{a}}_n$ are composed of the first three \mathbf{a}_n components without the forth ones for ϕ). With $d = 1 \text{ C/m}$, the displacement vector \mathbf{u} of the wavefield caused by this source is, in fact, the displacement part of the forth column \mathbf{k}_4 of Green's matrix $k(\mathbf{x})$. As it might be expected, the amplitude patterns of Fig. 5 are very similar to those for K_n^2 in Fig. 4, at that the use of Eq. (20) for the GW power estimation seems to be more advantageous. First, it does not require to derive and calculate one more solution for the auxiliary short-circuited problem and, second, it automatically yields the source energy partition among the excited GWs.

The loss decrements δ_n associated with the complex sections of the first five even modes ($n = 2, 4, \dots, 10$) are shown in Fig. 6. The first PSAW (Sezawa mode, $n = 2$) has the smallest decrement δ_2 . Its pattern and value coincide with those obtained in Refs. 4 and 5, exhibiting the same two

points of zero minima $h/\lambda = 0.09$ and 0.15 . The bottom zoomed-in subplot of Fig. 6 demonstrates the presence of similar points of δ_n minima for the higher modes as well. The phase velocities c_n for these values h/λ are above the SAW velocities. All such points revealed for the modes considered and the corresponding values c_n , K_n^2 and A_n are collected in Table II.

C. Three-layer model

As noted above, the two- and three-layer models are substantially different in the values of the threshold velocity c_s . It implies that all former real (SAW) branches shown in Fig. 3 become formally complex in the AlN/Diamond/ γ -TiAl three-layer model. Nevertheless, with a sufficiently large ratio H/h , the pattern of former real dispersion curves remains practically the same as in the $M=2$ case (compare Figs. 3 and 7 for $H/h=10$). The losses δ_n of these former SAWs are also negligible.

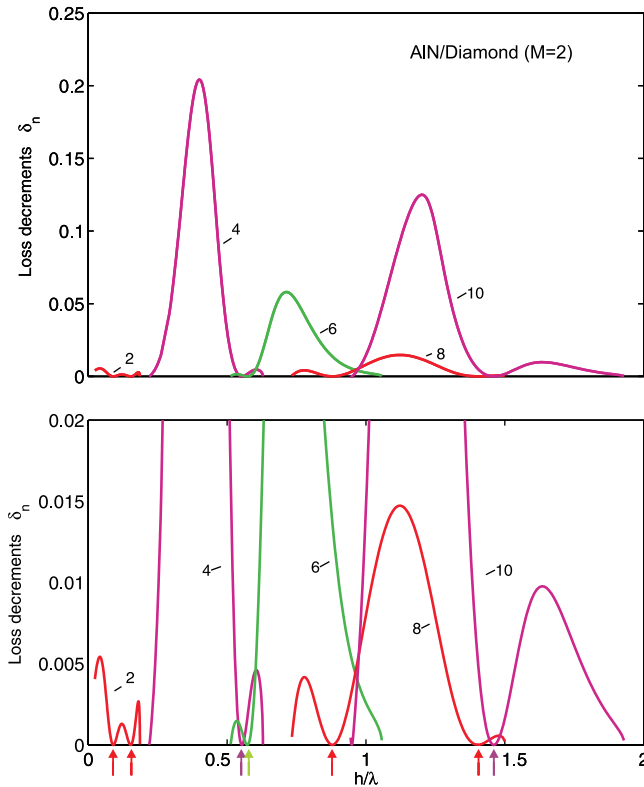


FIG. 6. Loss decrements δ_n for the first five PSAWs in AlN/Diamond structure (top), the bottom zoomed-in subplot demonstrates the presence of δ_n minima points (indicated by arrows) at which the PSAWs propagate as SAWs.

TABLE II. Points of PSAW-to-SAW degeneration ($M=2$).

h/λ	n	c_n (km/s)	K_n^2 (%)	A_n ($\mu\text{m} \cdot \text{m/C}$)
0.090	2	15.96	0.022	1.37
0.153	2	13.34	0.212	5.72
0.553	4	13.37	0.240	6.87
0.573	6	17.80	0.148	1.45
0.882	8	16.73	0.002	0.27
1.401	8	12.79	0.075	1.60
1.460	10	14.64	0.117	3.03

The only exception is in the low-frequency range in which the wavelength λ becomes larger than the diamond layer thickness H . The influence of the underlying metallic half-space increases and becomes decisive as $h/\lambda \rightarrow 0$. It appears in the down turn of the first (Rayleigh) branch in Fig. 7. Now, it tends to the Rayleigh wave velocity $c_R = 5608$ m/s of the γ -TiAl half-space instead of $c_R = 10920$ m/s in the $M=2$ case. Other complex poles ζ_n go up in the complex plane as $h/\lambda \rightarrow 0$ and the corresponding loss decrements δ_n rapidly grow. The terms \mathbf{u}_n in Eq. (20) associated with such poles

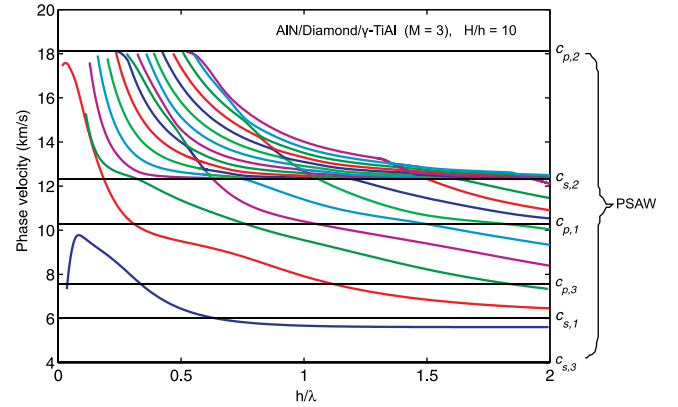


FIG. 7. PSAW dispersion curves for the three-layer structure with a relatively thick diamond interlayer: $H/h=10$.

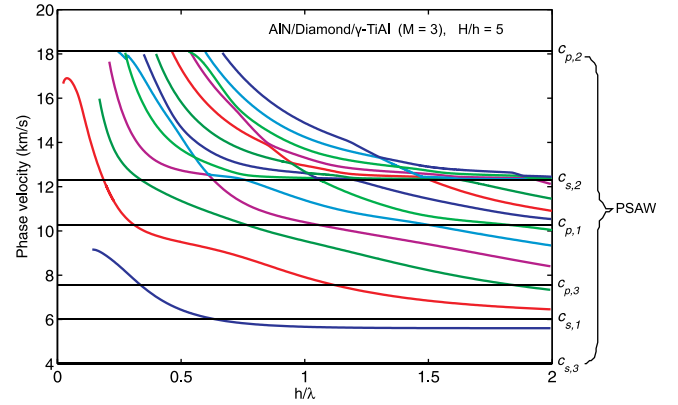


FIG. 8. The same as in Fig. 7 but for sublayers of thickness ratio $H/h=5$.

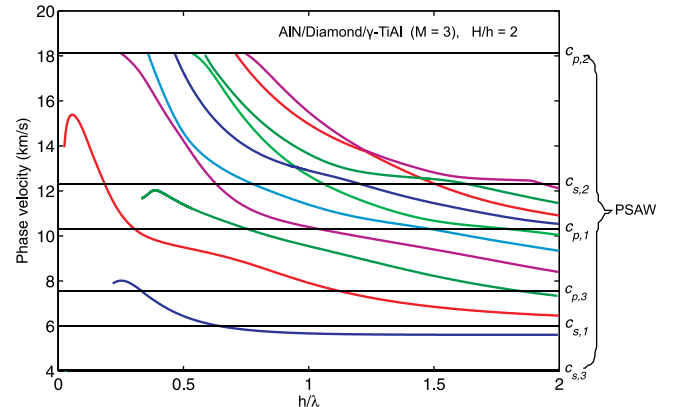


FIG. 9. The same as in Figs. 7 and 8 but for sublayers of comparable thicknesses: $H/h=2$.

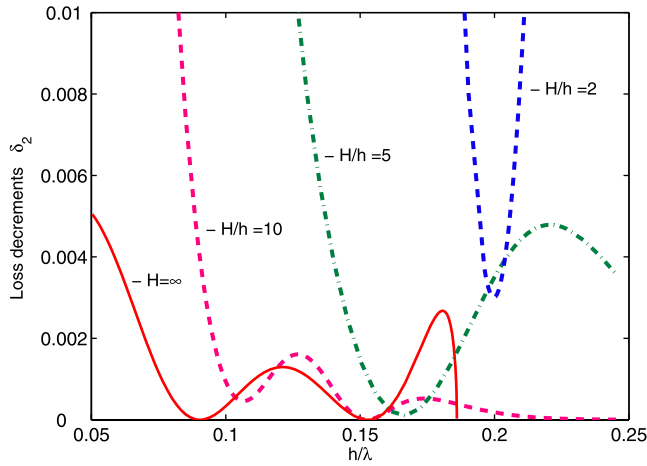


FIG. 10. Sezawa mode attenuation in different structures illustrating the change of optimal h/λ values with H/h variation.

could hardly be treated as guided waves. Therefore, the tracing of dispersion curves in Figs. 7–9 is stopped when their imaginary parts transcend certain large level in the course of h/λ decreasing.

With a smaller H/h ratio, the range of such substrate influence enlarges, appearing in a visible shape deformation of several next branches in addition to the first one (see Figs. 8 and 9 for $H/h=5$ and 2, respectively). Based on Fig. 9, one can conclude that the range of visible difference is at least $0 < h/\lambda < 0.5$ for $H/h=2$. In terms of H , it corresponds to the range $0 < H/\lambda < 1$. In other words, it confirms the assumption that the difference becomes noticeable when the wavelength λ is greater than H .

Thus, the values $h/\lambda = 0.09$ and 0.15 , being optimal for Sezawa wave generation in the AlN/Diamond structure, may essentially change if the underlying substrate is taken into account. Indeed, Fig. 10 depicting δ_2 plots for

$H/h = \infty, 10, 5$ and 2 demonstrates such a change. One can see that the point $h/\lambda = 0.09$ cease to be optimal in the three-layer case, while the optimal point $h/\lambda = 0.15$ is much more stable. It gradually shifts, however, to the right as H/h decreases and reaches the value $h/\lambda = 0.2$ when $H/h=2$.

One more consequence of the branch point change is that all the poles, being now complex, lie on the physical surface sheet. In particular, now the odd ones also continuously pass the former branch point level $c_{s,2} = 12\,320$ m/s keeping their contribution into GW expansion (20). Here, whereas the pattern of the former SAWs does not visibly vary for $H/\lambda > 1$, the shape of PSAW curves above $c_{s,2}$ drastically depends on the H/h ratio. The larger H/h is, the closer those curves nestle to the $c_{s,2}$ level just after its crossing as h/λ decreases. In addition, they exhibit sharp skew-step windings along the former PSAW trajectories that were actual in the $M=2$ case. Such pseudo-curves formed from the skew-step windings are well visible in Fig. 7 for the former 4th, 6th and, in part, 8th and 10th PSAW modes. The latter has appeared just in part because only the first 17 modes are presented in Fig. 7, while a lot of PSAW curves that would fill in the blank domain between the $c_{s,2}$ and $c_{p,2}$ levels are not shown there.

Meanwhile, the regularity of the step-like patterns is depicted by the zoomed-in subplots of Fig. 11. The loss decrement curves also exhibit a series of downward excursions in those ranges, which are more and more regular for higher modes (Fig. 12). Not all of those δ_n depressions reach down to the bottom zero level. However, as in the $M=2$ case, there also exist values of h/λ at which δ_n of certain PSAWs with phase velocities $c_n > c_{s,2}$ are small enough for treating them as SAWs. Some of such points are shown in Table III. It is noteworthy that the resonance nature of such points manifests itself not only in essential decreasing of the leakage loss but also in a sharp amplitude growth. The plots of

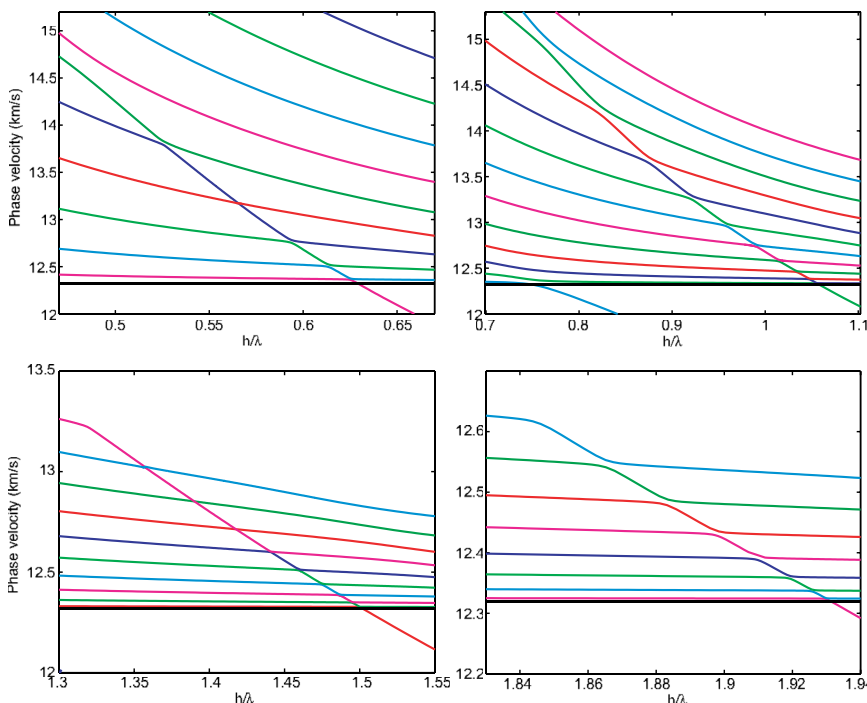


FIG. 11. Zoomed-in parts of dispersion curves in the case $H/h=10$ (Fig. 7) illustrating skew-step windings along the former PSAW trajectories.

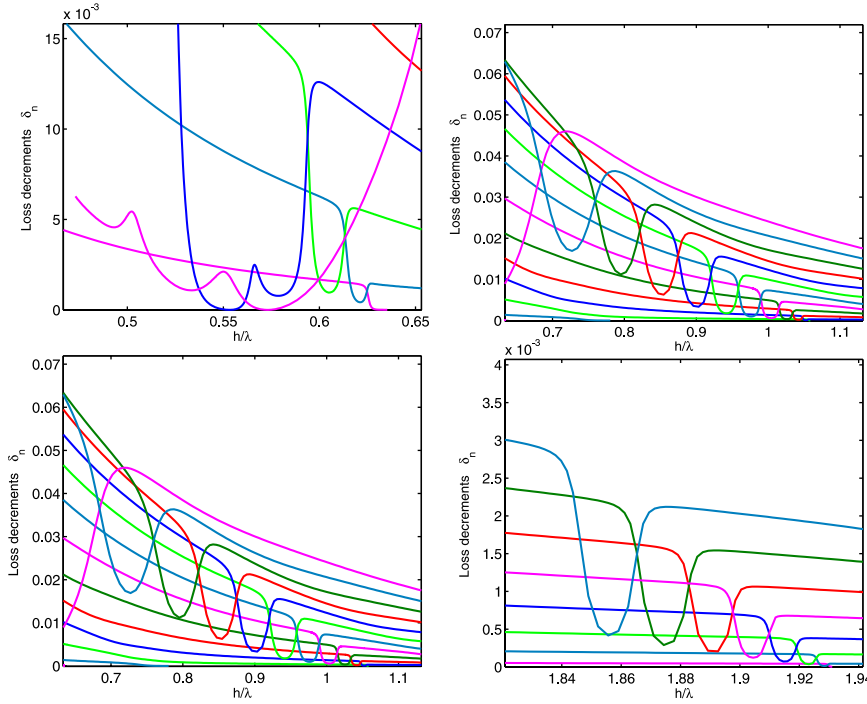


FIG. 12. Sharp loss decrement depressions at the skew-step sections shown in Fig. 11.

TABLE III. Points of PSAW-to-SAW degeneration ($M = 3$).

h/λ	n	$c_n(\text{km/s})$	$K_n^2(\%)$	$A_n(\mu\text{m} \cdot \text{m/C})$
$H/h = 10$				
0.152	2	13.36	0.206	5.63
0.553	7	13.36	0.239	6.88
0.573	16	17.80	0.148	1.44
1.042	8	12.42	0.013	0.84
1.401	16	12.79	0.075	1.60
1.447	13	12.57	0.066	1.58
$H/h = 5$				
0.167	2	12.90	0.293	6.88
0.554	5	13.35	0.240	6.89
1.036	7	12.46	0.011	0.81
1.403	11	12.79	0.075	1.60
$H/h = 2$				
0.200	2	11.97	0.531	9.00
0.553	4	13.37	0.240	6.90
0.882	10	16.73	0.002	0.26
1.401	8	12.79	0.075	1.60

the GW amplitudes $|\mathbf{u}_n|$ versus h/λ are featured by narrow peaks rising up at these points.

V. CONCLUSIONS

The integral equation based mathematical model for surface and pseudo-surface wave excitation and propagation in a high-velocity (diamond) isotropic layer covered by a piezoelectric film has been developed and implemented. In addition to wave characteristics provided by conventional modal expansions, the model strictly accounts for the wave source yielding specific SAW/PSAW amplitudes. The input material parameters may be quite general, thus the model is suitable for a wide range of layered piezo-electromechanical

structures. The PSAW modes in the AlN/Diamond/ γ -TiAl structure have been analyzed to clear up a possibility of their potential applications in high frequency SAW devices.

ACKNOWLEDGMENTS

This work has been initiated and conducted within the joint research project supported by the German Research Foundation (DFG, Project No. ZH 15/16-1) and also partly supported by the RFBR Grant No. 11-01-96509, which are gratefully acknowledged.

- ¹H. Nakahata, K. Higaki, S. Fujii, A. Hachigo, H. Kitabayashi, K. Tanabe, Y. Seki, and S. Shikata, in *IEEE Ultrasonics Symposium* (1995), pp. 361–370.
- ²O. Elmazria, F. Bénédict, M. El Hakiki, H. Moubchir, M. B. Assouar, and F. Silva, *Diamond Relat. Mater.* **15**(2–3), 193–198 (2006).
- ³M. Benetti, D. Cannatà, F. Di Pietrantonio, and E. Verona, *IEEE Trans. Ultrason. Ferroelectr. Freq. Control* **52**, 1806 (2005).
- ⁴M. Benetti, D. Cannatà, F. Di Pietrantonio, V. I. Fedosov, and E. Verona, in *IEEE Ultrasonics Symposium* (2005), p. 1868.
- ⁵M. Benetti, D. Cannatà, F. Di Pietrantonio, V. I. Fedosov, and E. Verona, *Appl. Phys. Lett.* **87**, 033504 (2005).
- ⁶M. Benetti, D. Cannatà, F. Di Pietrantonio, V. I. Fedosov, and E. Verona, in *IEEE Ultrasonics Symposium* (2006), pp. 2318–2321.
- ⁷M. B. Assouar, O. Elmazria, P. Kirsch, P. Alnot, V. Mortet, and C. Tiusan, *J. Appl. Phys.* **101**, 114507 (2007).
- ⁸S. Wu, R. Ro, Z. X. Lin, and M. S. Lee, *J. Appl. Phys.* **104**, 064919 (2008).
- ⁹S. Wu, R. Ro, and Z. X. Lin, *Appl. Phys. Lett.* **94**, 032908 (2009).
- ¹⁰L. M. Gao, Ch. Zhang, Z. Zhong, C.-P. Fritzen, X. Jiang, H.-J. Christ, and U. Pietsch, in *IUTAM Symposium on Multiscale Modelling of Fatigue, Damage and Fracture in Smart Materials IUTAM Bookseries* (2011), Vol. 24, pp. 207–217.
- ¹¹H. Engan, K. A. Ingebrigtsen, and A. Tønning, *Appl. Phys. Lett.* **10**, 311–313 (1967).
- ¹²E. Glushkov, N. Glushkova, and A. Eremin, *J. Acoust. Soc. Am.* **129**(5), 2923–2934 (2011).
- ¹³H. F. Tiersten, *Ultrasonics* **8**(1), 19–23 (1970).
- ¹⁴K. A. Ingebrigtsen, *J. Appl. Phys.* **40**, 2681–2686 (1969).
- ¹⁵E. Glushkov, N. Glushkova, O. Kvasha, and W. Seemann, *Smart Mater. Struct.* **16**, 650 (2007).
- ¹⁶E. L. Adler, *IEEE Trans. Ultrason. Ferroelectr. Freq. Control* **41**, 876 (1994).